Article:

Qin, Y., Li, G.-J. orcid.org/0000-0002-5956-4033, Zhu, Z.Q. et al. (4 more authors) (2025) Model-based Luenberger state observer for detecting interturn short-circuits in PM machines. IEEE Transactions on Transportation Electrification, 11 (2). pp. 5302-5311. ISSN 2332-7782

https://doi.org/10.1109/TTE.2024.3478840

Model-based Luenberger State Observer for Detecting Interturn Short-Circuits in PM Machines

Y. Qin, *Student Member, IEEE*, G. J. Li, *Senior Member, IEEE,* Z. Q. Zhu*, Fellow, IEEE,* M. P. Foster, D. A. Stone, C. J. Jia, and P. McKeever

***Abstract*—This paper proposes a novel model-based Luenberger state observer for interturn short-circuit (ITSC) fault diagnostics. The residuals between the observed currents and the measured currents in the α- and β-axes serve as fault indicator, which can be used to detect ITSC faults not only at an early stage with contact resistance but also at the fully short-circuited stage. These currents are observed by the Luenberger observer, which is designed under the assumption that the machine is operating in a healthy condition. In addition, the investigation results indicate that with greater fault ratio, larger load current and higher speed, detecting the ITSC fault becomes easier. Moreover, three sets of Luenberger observers, assuming the ITSC fault is in phases A, B, and C, respectively, have been designed to identify the faulted phase. A series of experiments have been carried out to validate the developed fault detection method.**

***Keywords*—fault detection, interturn short-circuit, Luenberger observer, PM machine, PWM.**

I. INTRODUCTION

INTER-turn short-circuit (ITSC) fault is one of the most common and serious faults in electrical machines. This is because ITSC fault accounts for approximately 30-40% [1] of total failures in electrical machines, generating fault currents nearly 30 times of the rated current. This serious fault is primarily caused by insulation failures, which, in turn, result from factors such as high *dv*/*d*t [2], aging and environmental contamination [3]. In addition, the ITSC fault could escalate to phase-to-phase and phase-to-ground short-circuits, leading to the breakdown of the entire machine [4]. Furthermore, the large fault current associated with ITSC faults could cause magnet irreversible demagnetization [5]. Given these potential risks posed by ITSC faults, they have attracted increasing attention both in academia and industry. The research on ITSC faults primarily focuses on three aspects: (1) fault modeling, (2) fault detection, and (3) fault mitigation strategies. Fault modeling enables an understanding of the electrical performances, facilitating the evaluation of consequences resulting from this serious fault [6]. Moreover, with an accurate fault model, theoretical support can be provided for designing machines with better fault tolerant capability [7]. Additionally, model-based fault diagnostic methods can be employed to detect this serious fault. In safety-critical applications, such as offshore wind generators, electric vehicles, and aerospace systems, early detection of faults, especially at their incipient stage, is extremely important [8]. Furthermore, timely detection allows for subsequent mitigation measures. Fault mitigation represents the final step, helping improve the fault tolerant capability of the system [9].

Based on the literature review, the fault detection methods could be divided into three categories: model-based, signal-based, and data-driven-based [10]. In [11], the fault models have been firstly established, then the negative-sequence current and the second order harmonic in the q-axis current are used as fault indicators for ITSC fault detection. However, the effectiveness of this detection method may be significantly compromised in the drive systems with field-oriented control (FOC) and current regulators, as they can compensate the unbalance in the phase currents [12]. To enhance the detection sensitivity, an alternative approach utilizes zero-sequence voltage [13] and current [14] as fault indicators. However, this approach has limitations, requiring access to the neutral point of the phase windings and necessitating additional voltage sensors, thereby adding complexity to the system. Consequently, these limitations impact the widespread application of this approach. The model-based high frequency (HF) voltage injection methods have also been used for fault detection [2] [15] [16]. However, due to the injected voltage, the generated HF currents will produce extra torque ripple and thermal stress, imposing additional burdens on the normal operation of the system. In [17], HF rotating current injection is integrated with zero-sequence voltage components (ZSVC) to detect and differentiate between ITSC fault and resistance unbalance faults. However, the frequency of the HF rotating current injection is constrained to several hundred Hz due to the limited bandwidth of the HF current regulator. This constraint hinders the ability to achieve high-resolution ITSC fault detection using the HF rotating current injection technique.

The signal-based fault detection methods use spectral tools to detect changes in signals, such as stator phase current [3], zero sequence current component (ZSCC) [18], and zero sequence voltage component (ZSVC) [19]. However, this approach, to some extent, may lead to false alarms, as with few turns being short-circuited, the spectrum exhibits negligible differences from the healthy conditions. As technologies progress, some data-driven approaches have emerged as alternative for fault detection [20]. Various data-driven approaches leveraging artificial intelligence (AI) have emerged for detecting ITSC faults in electrical machines. AI-based methodologies offer several advantages over traditional diagnostic approaches. They generally demonstrate enhanced performance when finely tuned, are easily scalable and customizable, and can be adjusted by integrating new data or information as it becomes accessible [21]. Additionally, their design does not necessarily require a comprehensive mathematical model of the machine, which may not be available in certain scenarios. These methods employ diverse techniques for fault diagnosis, with common approaches including expert systems, artificial neural networks (ANNs), and fuzzy logic [22]. However, the collection of extensive historical data under various fault levels and operating conditions is necessary. Owing to its reliance on powerful computing capabilities, this approach faces limitations in achieving widespread application.

Recently, some researchers have attempted to use Luenberger observer (often used for sensorless control in electrical machines [23]) for ITSC fault detection. For example, in [24], the Luenberger observer is utilized to estimate the d- and q-axes currents, and subsequently, the 2[nd] order harmonics of residual components between the measured and estimated d- and q-axes currents are employed as fault indicators. This approach can effectively detect the ITSC faults and evaluate the fault severity. However, it cannot locate the faulty phase. In [25], the Luenberger observer is designed to estimate the d- and q-axes resistance, which can be utilized to calculate the d- and q-axes voltages. The second harmonics of the d- and q-axes voltages can be considered as the fault indicator. However, again, this approach cannot identify the faulted phase. In [26], the Luenberger observer has been employed in the doubly-fed induction generator to detect ITSC faults. The residuals between the observed and measured phase currents serve as the fault indicator. However, the faulted phase identification strategy has not been elaborated. To obtain fault ratio in the machine, a large number of Luenberger observers (>>3) have been designed and executed in parallel. While this method is feasible in MATLAB simulation, it is difficult to be implemented in practice. This is because executing multiple Luenberger observers in parallel requires the micro controller unit (MCU) to have the same number of cores as the number of observers. This is nearly impossible. For instance, the Infineon TC275 MCU, utilized in the EV, has only three cores, far less than the required number of observers. In addition to the Luenberger observer, the extended Kalman filter, though not the focus of this paper, is another main approach used to estimate the state vectors, and it has also been employed for detecting ITSC faults in electrical machines [27].

To address the above shortcomings, this paper proposes a novel model-based Luenberger state observer for detecting ITSC faults in PM machines. The proposed fault model facilitated the development of a full-order Luenberger observer, characterized by a robustly designed gain matrix $\boldsymbol{L}$ that effectively handles variations in parameters of the state matrix $\boldsymbol{A}$, including the fluctuations in rotor speed and fault ratio. The residuals between the observed currents and the measured α- and β-axes currents are utilized as fault indicators, which can be used to detect ITSC faults at both the early stage, characterized by a non-zero contact resistance, and the fully short-circuited stage (zero contact resistance). These observed currents are obtained from the Luenberger observer. In addition, only three Luenberger observers, one for each phase, are needed to determine the faulty phase.

The rest of this paper is structured as shown in Fig. 1. In section 0, a PWM-voltage-based model for PM machines under ITSC fault is developed, the full-order Luenberger observer is investigated, and the gain matrix $\boldsymbol{L}$ for the Luenberger observer is designed. In section III, the fault detection strategy is explored, the proposed detection method is validated under both non-zero and zero contact resistance, and the main factors influencing the residuals, such as fault ratio, speed, and load current, are analyzed. In section IV, faulted phase identification

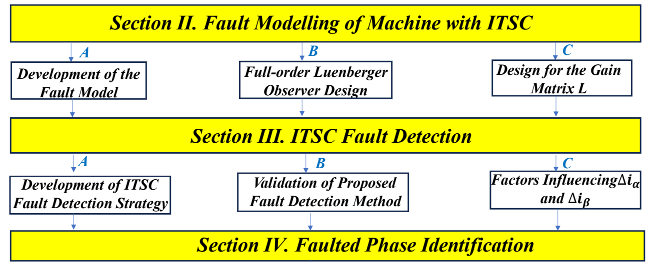

Fig. 1 Flowchart summarizing the main structure of this paper.

strategy is explored and validated. Finally, some conclusions are drawn in section V.

TABLE I PARAMETERS OF PM MACHINE WITH ITSC FAULT

Nº of phases	3	Phase resistance (mΩ)	7.780
Nº of poles/slots	8/6	Phase inductance (μH)	300
Nº of turns per coil	24	PM flux (mWb)	5.94
Rated power (W)	30	Rated torque (Nm)	0.6
Rated speed (rpm)	500	Rated phase current (A)	16
Maximum speed (rpm)	1500	Maximum power (W)	200

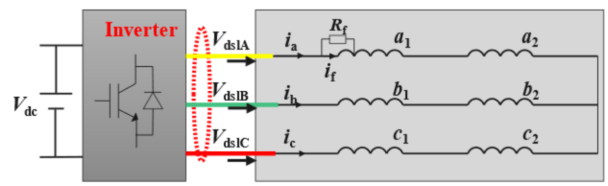

Fig. 2 PMSM with series connected coils under ITSC fault in phase A.

II. Fault Modelling of Machines with ITSC

A. Development of the Fault Model

It can be seen from Fig. 2 that each phase winding is composed of two coils. The key parameters for the investigated machine are shown in TABLE I. For the fault modelling, unless stated otherwise, it is assumed that the ITSC fault occurs in coil a_1. Using Kirchhoff's Voltage Law (KVL), the relationship between the inputs (PWM voltages) and the state variables (three-phase currents and fault current) can be described as (1). Using Kirchhoff's Current Law (KCL), the neutral point voltage (v_{n}) can be expressed as (2).

$$\boldsymbol{L_{ind}}\frac{d}{dt}\begin{bmatrix} i_a \\ i_b \\ i_c \\ i_f \end{bmatrix} = -\boldsymbol{R}\begin{bmatrix} i_a \\ i_b \\ i_c \\ i_f \end{bmatrix} + \begin{bmatrix} v_{dslA} \\ v_{dslB} \\ v_{dslC} \\ 0 \end{bmatrix} - \begin{bmatrix} e_{ah} \\ e_b \\ e_c \\ e_{af} \end{bmatrix} - \begin{bmatrix} 1 \\ 1 \\ 1 \\ 0 \end{bmatrix} v_n \tag{1}$$

$$v_{\mathrm{n}} = -\frac{1}{3}\begin{bmatrix} 1 \\ 1 \\ 1 \\ 0 \end{bmatrix}^T \left\{ \boldsymbol{L_{ind}}\frac{d}{dt}\begin{bmatrix} i_a \\ i_b \\ i_c \\ i_f \end{bmatrix} + \boldsymbol{R}\begin{bmatrix} i_a \\ i_b \\ i_c \\ i_f \end{bmatrix} - \begin{bmatrix} v_{dslA} \\ v_{dslB} \\ v_{dslC} \\ 0 \end{bmatrix} + \begin{bmatrix} e_{ah} \\ e_b \\ e_c \\ e_{af} \end{bmatrix} \right\} \tag{2}$$

with

$$\begin{cases} \boldsymbol{R} = \begin{bmatrix} R_{s11} & 0 & 0 & R_{s14} \\ 0 & R_{s22} & 0 & 0 \\ 0 & 0 & R_{s33} & 0 \\ R_{s41} & 0 & 0 & R_{s44} \end{bmatrix} \\ \boldsymbol{L_{ind}} = \begin{bmatrix} L_{s11} & M_{s12} & M_{s13} & M_{s14} \\ M_{s21} & L_{s22} & M_{s23} & M_{s24} \\ M_{s31} & M_{s32} & L_{s33} & M_{s34} \\ M_{s41} & M_{s42} & M_{s43} & L_{s44} \end{bmatrix} \\ e_{ah} = (1-\mu/2)e_a, \text{and } e_{af} = \mu/2 e_a \end{cases} \tag{3}$$

where $\boldsymbol{R}$ and $\boldsymbol{L_{ind}}$ are 4×4 resistance and inductance matrices, respectively. R_{s11} is the sum of the healthy winding resistance of phase A and the contact resistance R_f, while R_{s44} is the sum of the faulted turns resistance of phase A and the contact resistance R_f. The values of R_{s14} and R_{s41} are equal to $-R_f$ due to the coupled electrical circuits between the healthy turns and faulted turns at the incipient stage of the ITSC fault. R_{s22} and R_{s33} are the resistances of phases B and C. e_{ah} and e_{af} represent the back-EMF of the healthy and faulted turns in phase A, e_a, e_b and e_c are the back-EMFs of phases A, B and C, respectively. The output signals from the inverter are labelled as V_{dslA}, V_{dslB} and V_{dslC}. $\mu = N_{fault}/N$ is the faulted turn ratio of coil a_1, where N_{fault} and N are the numbers of faulted turns and total turns of the a_1 coil, respectively. L_{s11} and L_{s44} are the inductances of the healthy and faulted turns in phase A, L_{s22} and L_{s33} represent the total self-inductances of phases B and C, respectively. M_{s12} and M_{s21} are the mutual inductances between the healthy winding of phases A and B, M_{s13} and M_{s31} are the mutual inductances between the healthy winding of phases A and C, and M_{s14} and M_{s41} are the mutual inductances between the healthy winding and faulted winding of phase A. M_{s23} and M_{s32} are the mutual inductances between phases B and C. M_{s24} and M_{s42} are the mutual inductances between phase B and short-circuited windings of phase A, while M_{s34} and M_{s43} are the mutual inductances between phase C and short-circuited winding of phase A.

According to the work presented in [28], the analytical fault model in α-and β- axes could be derived as (4).

$$\frac{d}{dt}\begin{bmatrix} i_\alpha \\ i_\beta \\ i_f \end{bmatrix} = \boldsymbol{L^{-1}_{3\times3}} \times \boldsymbol{R_{3\times3}} \begin{bmatrix} i_\alpha \\ i_\beta \\ i_f \end{bmatrix} + \boldsymbol{L^{-1}_{3\times3}}\left(\begin{bmatrix} v_\alpha \\ v_\beta \\ v_f \end{bmatrix} - \begin{bmatrix} e_\alpha \\ e_\beta \\ e_f \end{bmatrix}\right) \tag{4}$$

with

$$\boldsymbol{L_{3\times3}} = \begin{bmatrix} \frac{2L_{s11}+2L_{s22}-4M_{s12}+M_{s23}}{3} & 0 & \frac{2M_{s14}-2M_{s24}}{3} \\ 0 & L_{s22}-M_{s23} & 0 \\ M_{s14}+\frac{M_{s34}-M_{s24}}{2} & 0 & L_{s44} \end{bmatrix} \tag{5}$$

$$\boldsymbol{R_{3\times3}} = \begin{bmatrix} -\frac{2R_{s11}}{3}-\frac{R_{s22}}{3} & 0 & -\frac{2R_{s14}}{3} \\ 0 & -R_{s22} & 0 \\ -R_{s14} & 0 & -R_{s44} \end{bmatrix} \tag{6}$$

$$\begin{bmatrix} S_\alpha \\ S_\beta \\ S_f \end{bmatrix} = \begin{bmatrix} \frac{2}{3} & -\frac{1}{3} & -\frac{1}{3} & 0 \\ 0 & \frac{\sqrt{3}}{3} & -\frac{\sqrt{3}}{3} & 0 \\ 0 & 0 & 0 & 1 \end{bmatrix} \begin{bmatrix} S_a \\ S_b \\ S_c \\ S_f \end{bmatrix} \tag{7}$$

where S can be voltage (v), back-EMF and current (i).

B. Full-Order Luenberger Observer Design

Based on the proposed fault model, as presented in (4), a new state vector $[i_\alpha \quad i_\beta \quad i_f \quad e_\alpha \quad e_\beta]^T$ has been selected. As a result, the state-space representation for (4) can be transformed into (8). In comparison with (4), the back-EMFs in α- and β-axes have also been considered as part of the state vector. Consequently, the back-EMF can be observed in the designed full-order Luenberger observer.

$$\frac{d}{dt}\begin{bmatrix} i_\alpha \\ i_\beta \\ i_f \\ e_\alpha \\ e_\beta \end{bmatrix} = \boldsymbol{A}\begin{bmatrix} i_\alpha \\ i_\beta \\ i_f \\ e_\alpha \\ e_\beta \end{bmatrix} + \boldsymbol{B}\begin{bmatrix} v_\alpha \\ v_\beta \end{bmatrix} \text{and} \begin{bmatrix} i_\alpha \\ i_\beta \end{bmatrix} = \boldsymbol{C}\begin{bmatrix} i_\alpha \\ i_\beta \\ i_f \\ e_\alpha \\ e_\beta \end{bmatrix} \tag{8}$$

with

$$\boldsymbol{A} = \begin{bmatrix} \underbrace{\boldsymbol{L^{-1}_{3\times3}} \times \boldsymbol{R_{3\times3}}}_{3\times3} & \underbrace{-\boldsymbol{L^{-1}_{3\times3}} \times \begin{bmatrix} 1 & 0 \\ 0 & 1 \\ \frac{\mu}{2-\mu} & 0 \end{bmatrix}}_{3\times2} \\ \underbrace{\boldsymbol{0_{2\times3}}}_{2\times3} & \underbrace{\begin{bmatrix} 0 & -\left(1-\frac{1}{2}\mu\right)\omega \\ \frac{1}{\left(1-\frac{1}{2}\mu\right)}\omega & 0 \end{bmatrix}}_{2\times2} \end{bmatrix} \tag{9a}$$

$$\boldsymbol{B} = \begin{bmatrix} \underbrace{\boldsymbol{L^{-1}_{3\times3}} \times \begin{bmatrix} 1 & 0 \\ 0 & 1 \\ 0 & 0 \end{bmatrix}}_{3\times2} \\ \underbrace{\boldsymbol{0_{2\times2}}}_{2\times2} \end{bmatrix} \text{and } \boldsymbol{C} = \begin{bmatrix} 1 & 0 & 0 & 0 & 0 \\ 0 & 1 & 0 & 0 & 0 \end{bmatrix} \tag{9b}$$

where ω is the electrical angular velocity of the PM machine. $\boldsymbol{0_{2\times3}}$ and $\boldsymbol{0_{2\times2}}$ are 2×3 and 2×2 zero matrices, respectively.

Luenberger observer operates by comparing the actual system output, represented by measurable signals (i_α and i_β), with the output ($\widehat{i_\alpha}$ and $\widehat{i_\beta}$) predicted by the designed Luenberger observer shown in Fig. 3. Based on the difference (or residual) between the predicted and actual outputs, the estimated output can be automatically adjusted. The observer incorporates feedback of the measurable states to continually refine its estimates, thereby enhancing the accuracy of state estimation. The Luenberger observer is characterized as a dynamical system, as described by (10).

$$\begin{cases} \dot{\hat{x}} = \boldsymbol{A_{est}}\hat{x} + \boldsymbol{L}(y-\hat{y}) + \boldsymbol{B_{est}}u \\ \hat{y} = \boldsymbol{C}\hat{x} \end{cases} \tag{10}$$

where $\boldsymbol{A_{est}}$ is the estimated state matrix, $\boldsymbol{B_{est}}$ is the estimated input matrix, $\boldsymbol{C}$ is the output matrix and $\boldsymbol{L}$ is the Luenberger gain matrix. u ($[v_\alpha \quad v_\beta]^T$) are the inputs, $\hat{x}$ ($[\widehat{i_\alpha} \quad \widehat{i_\beta} \quad \widehat{i_f} \quad \widehat{e_\alpha} \quad \widehat{e_\beta}]^T$) are the estimated state vectors and y and $\hat{y}$ are the measured and estimated currents in α- and β-axes. The matrices $\boldsymbol{A_{est}}$, $\boldsymbol{B_{est}}$ and $\boldsymbol{C}$ have been described in (9a).

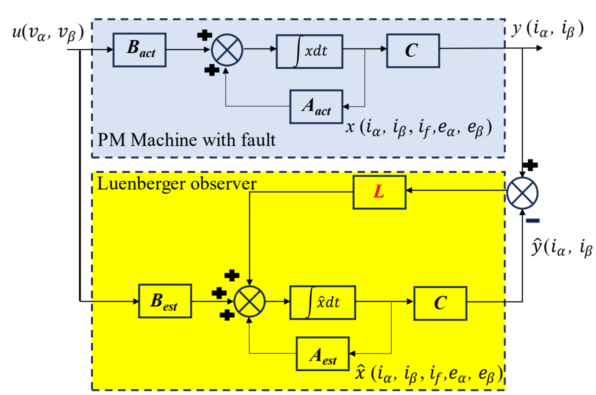

Fig. 3 Structural diagram of a full-state observer.

It can be observed from (9a) that the state matrix $\boldsymbol{A}$ and input matrix $\boldsymbol{B}$ are influenced by the fault ratio (μ), rotor speed which can be obtained by the speed sensors, and machine parameters such as phase resistance and inductance. In fact, one cannot ascertain the true state of the machine, i.e., whether the motor is in a healthy or faulty condition. This implies that, during the design of the observation system, the fault ratio (μ) cannot be determined. However, one could initially assume the machine is healthy, setting x to zero. Consequently, $\boldsymbol{A_{est}}$ and $\boldsymbol{B_{est}}$ can be determined. If the machine is indeed healthy, $\boldsymbol{A_{est}}$ and $\boldsymbol{B_{est}}$ for the Luenberger observer show no residuals compared to their actual counterparts, $\boldsymbol{A_{act}}$ and $\boldsymbol{B_{act}}$, representing the real state and input matrices for the machine. The estimated state vector residuals can be further derived, as shown in (11). It is found that if the designed gain matrix $\boldsymbol{L}$ could ensure that all eigenvalues of ($\boldsymbol{A}$-$\boldsymbol{LC}$) possess negative real parts, the residuals between the estimated state variables and the actual state variables could converge to zero within a finite time. This implies that there are no residuals between the estimated currents ($\widehat{i_\alpha}$ and $\widehat{i_\beta}$) and the measurable currents (i_α and i_β).

$$\Delta x(t) = e^{(\boldsymbol{A}-\boldsymbol{LC})}\Delta x_0 \tag{11}$$

with

$$\Delta x(t) = x(t) - \hat{x}(t) \text{ and } \Delta x_0 = x(0) - \hat{x}(0) \tag{12}$$

where Δx are the residuals between the state vector in the PM machine ($[i_\alpha \quad i_\beta \quad i_f \quad e_\alpha \quad e_\beta]^T$) and that in the designed observer ($[\widehat{i_\alpha} \quad \widehat{i_\beta} \quad \widehat{i_f} \quad \widehat{e_\alpha} \quad \widehat{e_\beta}]^T$). Δx_0 are the initial estimation residuals.

However, if the system is actually faulty, such as one turn being short-circuited, $\boldsymbol{A_{est}}$ and $\boldsymbol{B_{est}}$, determined under the assumption of a healthy condition, will exhibit residuals when compared to their counterparts $\boldsymbol{A_{act}}$ and $\boldsymbol{B_{act}}$. This residual arises from differences in the estimated μ used in the observer design and the actual μ present in the machine. Under this scenario, the residuals in the estimation state vector can be derived in more detail, as indicated in (13). It can be observed from (13) that under these conditions, there are residuals between the estimated currents ($\widehat{i_\alpha}$ and $\widehat{i_\beta}$) and the measurable currents (i_α and i_β).

$$\Delta\dot{x}(t) = (\boldsymbol{A_{act}} - \boldsymbol{LC})\Delta x(t) + \Delta\boldsymbol{B}u + \Delta\boldsymbol{A}\hat{x}(t) \tag{13}$$

with

$$\Delta x(t) = x(t) - \hat{x}(t), \Delta\boldsymbol{A} = \boldsymbol{A_{act}} - \boldsymbol{A_{est}} \text{ and } \Delta\boldsymbol{B} = \boldsymbol{B_{act}} - \boldsymbol{B_{est}} \tag{14}$$

C. Design for the Gain Matrix L

The selection of the observer gain matrix $\boldsymbol{L}$ necessitates ensuring that all eigenvalues of ($\boldsymbol{A_{act}} - \boldsymbol{LC}$) possess negative real parts. It is worth noting that the state matrix $\boldsymbol{A_{act}}$ for the machine with an ITSC fault is not only related to the rotor speed but also to the fault ratio (μ), as indicated in (9a). While rotor speed can be measured, μ in the machine is not known in advance. Due to the uncertainty regarding μ, $\boldsymbol{L}$ should be designed in such a way that, as x varies from 0 to 1 and the rotor speed changes from 0 rpm to the maximum rotational speed, all eigenvalues of ($\boldsymbol{A_{act}} - \boldsymbol{LC}$) exhibit negative real parts. Using the pole assignment method [29], the designed matrix $\boldsymbol{L}$, as seen in (15), ensures that all five eigenvalues of ($\boldsymbol{A_{act}} - \boldsymbol{LC}$) have negative real parts as x varies from 0 to 1, and the speed changes from 0rpm to the maximum speed (1500 rpm), as shown in Fig. 4. However, due to space limit, results for eigenvalues 2 to 5 are not shown here, but they are all negative, similar as eigenvalue 1.

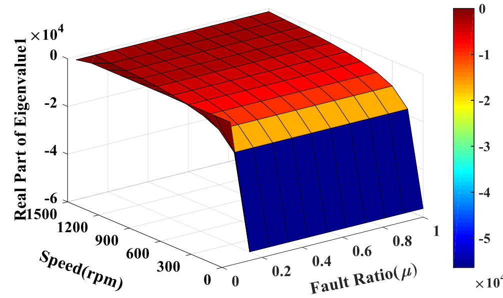

Fig. 4 Real part of eigenvalue 1 for $\boldsymbol{A}$-$\boldsymbol{LC}$ *vs* fault ratio (μ) and rotor speed.

$$\boldsymbol{L} = \begin{bmatrix} -138788 & -138788 \\ 141204 & 141204 \\ -116399 & -116399 \\ -6205 & -6205 \\ 1392 & 1392 \end{bmatrix} \tag{15}$$

III. ITSC Fault Detection

A. Development of ITSC Fault Detection Strategy

As discussed in section II.B, when the estimated μ is the same as the actual μ, the estimated matrices $\boldsymbol{A_{est}}$ and $\boldsymbol{B_{est}}$ will be identical to $\boldsymbol{A_{act}}$ and $\boldsymbol{B_{act}}$. As a result, in theory, there are no residuals between the observed $\widehat{i_\alpha}$ and $\widehat{i_\beta}$ and the measurable i_α and i_β; otherwise, $\widehat{i_\alpha}$ and $\widehat{i_\beta}$ would differ from i_α and i_β. It is evident that the initial assumption is that the machine is healthy, thereby setting μ to zero. If this holds true, the matrices $\boldsymbol{A_{est}}$ and $\boldsymbol{B_{est}}$ can be subsequently determined for the designed observer. The observed $\widehat{i_\alpha}$ and $\widehat{i_\beta}$ can then be obtained from the observer. To prevent false alarms, it is advisable to establish a threshold for $|\widehat{i_{\alpha\beta}} - i_{\alpha\beta}|$. An alarm should only be activated when this threshold is exceeded, which ensures precise fault detection and reduces the likelihood of false positives. This paper recommends a threshold of 0.015A, based on experimental calibration for the investigated machine. As a result, the fault detection strategy can be implemented, as shown in Fig. 5. If the residuals between the observed $\widehat{i_\alpha}$ and $\widehat{i_\beta}$ and the measurable i_α and i_β are lower than 0.015A, it can be concluded that the machine is healthy. Otherwise, the machine is experiencing an ITSC fault.

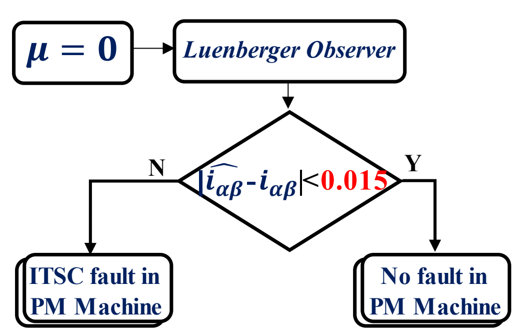

Fig. 5 Flowchart of ITSC fault detection. μ is fault ratio.

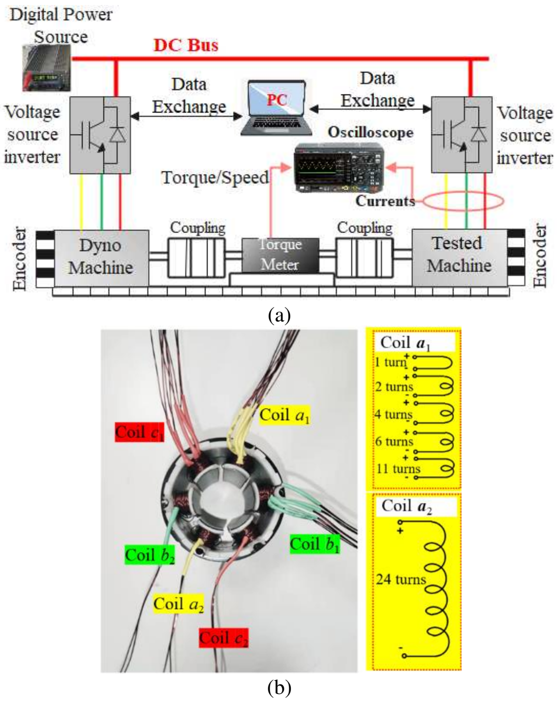

Fig. 6 Test setup with ITSC fault in the test PM machine. (a) Test rig. (b) Tested PM machine.

B. Validation of Proposed Fault Detection Method

To validate the proposed fault detection method, a series of simulations and measurements have been conducted. The simulated results were obtained using MATLAB/Simulink, while the measured results were acquired from the test rig shown in Fig. 6. The test rig comprises three main components: (1) dyno and test machines, (2) two sets of three-phase converters, and (3) a torque meter. The dyno machine provides stable speed for the system, while the tested machine operates in torque mode. Two sets of three-phase converters are employed to control the dyno and the tested machine separately. The torque meter is utilized to measure the torque and speed waveforms. As depicted in Fig. 6, the ITSC fault is simulated in the tested machine, where each phase winding is composed of two coils, and each coil consists of 24 turns. To introduce ITSC faults, coils a_1, b_1, and c_1 are each segmented into five sections, with each section having a different number of turns. This allows for the emulation of 1, 2, 4, 6, and 11 turns being short-circuited with thick cables (where the resistance is negligible) and a switch, facilitating the investigation of the influence of the zero impedance in the short-circuit path. Additionally, to simulate short-circuit faults with other different numbers of turns than those specified above, one can connect the above branches in series. For instance, to simulate a short-circuit fault with 12 turns, the branches corresponding to 1 turn and 11 turns can be connected in series, then the resultant branch can be short-circuited. Therefore, this flexible design allows for the simulation of short-circuit faults ranging from 1 to 24 turns. To simulate the initial stages of ITSC faults involving contact resistance, one approach is to configure series-connected resistors with varying resistance values across the branch. In both simulations and experiments, unless stated otherwise, the bus voltage is set to be 24V, the dead time is configured to be 0.5µs, and the switching frequency is 20kHz.

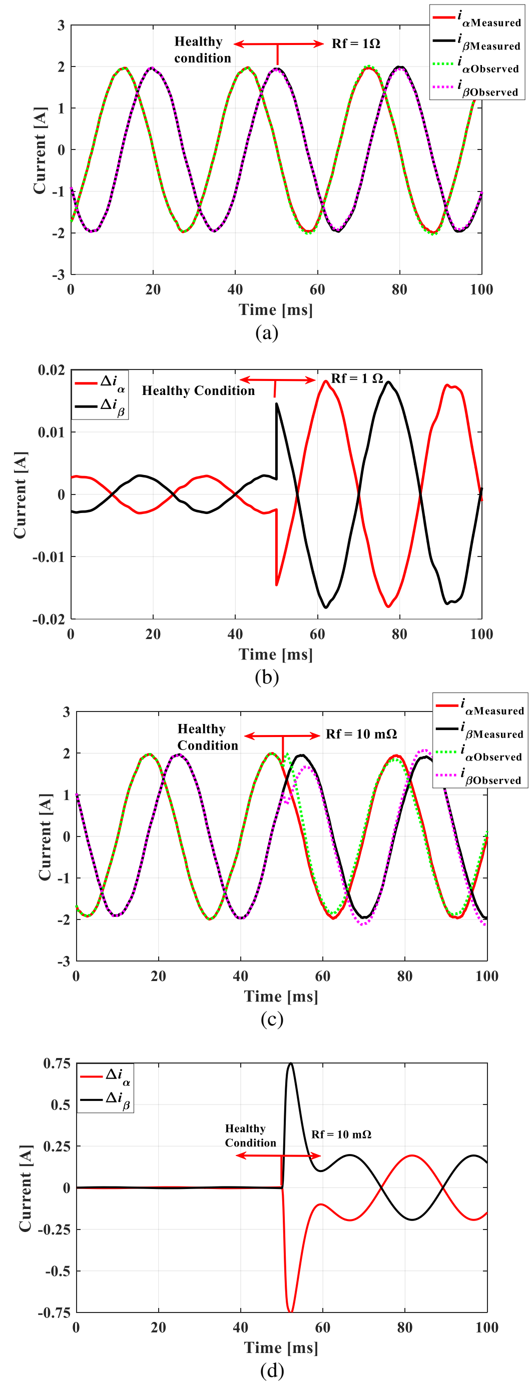

Fig. 7 Load currents are i_d = 0A and i_q = 2A, and the rotor speed is 500rpm. For healthy condition, $R_f = \infty$. For fault condition, μ=1/24. (a) Measured and observed i_α and i_β (R_f = 1Ω), (b) Δi_α and Δi_β (R_f = 1Ω), (c) Measured and observed i_α and i_β (R_f = 10mΩ), and (d) Δi_α and Δi_β (R_f = 10mΩ).

a. At Early Stage of ITSC ($R_f \neq 0$)

To simulate the initial behavior of ITSC faults, resistors with 1Ω and 10mΩ are respectively series-connected within the first branch of coil a_1, which consists of a single turn, to emulate the contact resistance. If the contact resistance is set to 1Ω, which is approximately 130 times larger than the phase resistance. In this case, the ITSC fault can be regarded as in its early stage, so the electrical performance of the machine remains very close to its healthy condition. Fig. 7 (a) and Fig. 7 (b) show that, under healthy condition, the deviations between the observed and measured currents are much smaller than the calibrated value (0.015A), as shown in Fig. 5. However, when an ITSC fault occurs at 50ms with the contact resistance of 10mΩ, deviations between the observed and measured currents begin to appear, resulting in the expected residuals (Δi_{α} and Δi_{β}). Fig. 7 (c) and Fig. 7 (d) demonstrate that when the contact resistance is set to 10mΩ, much larger residuals (Δi_{α} and Δi_{β}) compared to the contact resistance of 1Ω are observed, triggering the fault alarm.

b. At Fully Short-circuited Stage ($R_f = 0$)

The ITSC fault in phase A has been taken as an example, it can be observed from Fig. 8 (a) that under healthy conditions, the observed currents are identical to the measured ones. However, when the ITSC fault occurs at 50ms, the observed currents deviate from the measured ones, resulting in residuals (Δi_{α} and Δi_{β}), as expected. Fig. 8 (b) indicate that the greater the number of turns being short-circuited, the larger the amplitude of Δi_{α} and Δi_{β}, making fault detection more easily. Fig. 9 (a) and (b) illustrate that even with changes in speed or load current, the observed currents converge within finite time. This further demonstrates the robustness of the design gain matrix $\boldsymbol{L}$ for the Luenberger observer, as the state matrix $\boldsymbol{A}$ changes with variations in speed. However, residuals persist between the observed and measured currents after the ITSC fault.

C. Factors Influencing Δi_{α} and Δi_{β}

In this section, the factors that can influence Δi_{α} and Δi_{β} will be explored. It can be concluded from (13) that Δi_{α} and Δi_{β} are influenced by the deviation between the estimated μ and the actual μ in the electrical machine. This is because, the residual between the estimated μ and the actual μ introduces discrepancies in the matrices $\Delta\boldsymbol{A}$ and $\Delta\boldsymbol{B}$ [see (13)], making them unequal to the zero matrix. The larger the residual is, the greater the deviation of $\Delta\boldsymbol{A}$ and $\Delta\boldsymbol{B}$ from the zero matrix will be, resulting in larger Δi_{α} and Δi_{β}. This implies that when the observer is designed under the assumption that the machine has no faults, but the actual system has faults, deviations between the observed and measured currents will emerge. The greater x is, the larger Δi_{α} and Δi_{β} will be, as shown in Fig. 10.

With (13), a block diagram describing the residual model for Δi_{α} and Δi_{β} is depicted in Fig. 11. It is found that the structure of the residual model is similar to that of the PM machine (see Fig. 3). The input u, considered as the input for the PM machine, is also the input for the residual model. The state matrix for the residual model is represented by $(\boldsymbol{A_{act}} - \boldsymbol{LC})$, with $\Delta\boldsymbol{B}$ serving as the input matrix. The disturbances are denoted by $\Delta\boldsymbol{A}\hat{\boldsymbol{x}}$. Consequently, Δi_{α} and Δi_{β} can be influenced by the input u. In the case of the PM machine, higher load currents result in increased u. Similarly, higher speeds lead to larger u. Therefore, higher load currents or speed results in greater Δi_{α} and Δi_{β}, as shown in Fig. 12 and Fig. 13, making it easier to detect the ITSC faults.

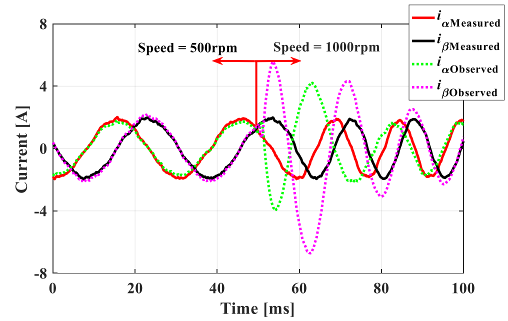

(a)

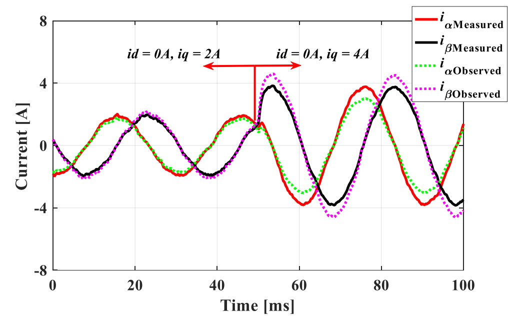

(b)

Fig. 9 Measured and observed i_{α} and i_{β} and μ is 0.5. (a) The rotor speed changes from 500rpm to 1000rpm at 50ms and the load currents are i_d = 0A, i_q = 2A, and (b) the load currents change from i_d = 0A, i_q = 2A to i_d = 0A, i_q = 4A at 50ms and the rotor speed is 500rpm.

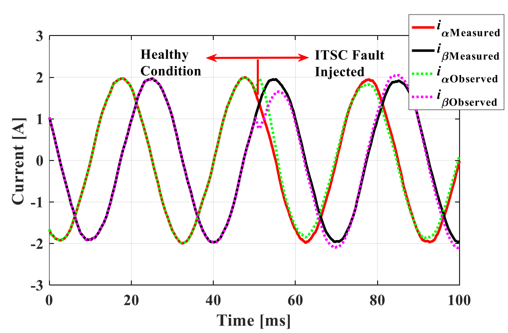

(a)

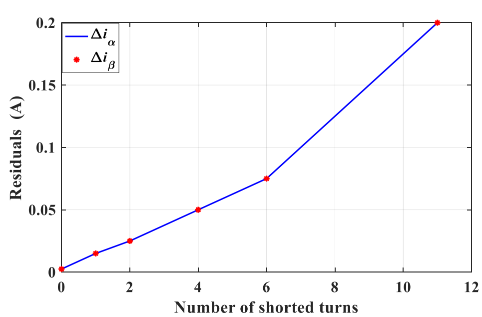

(b)

Fig. 8 Load currents are i_d = 0A and i_q = 2A, and the rotor speed is 500rpm. μ changes from 0 (healthy condition) to 0.5 at 50ms. (a) Measured and observed i_{α} and i_{β}, and (b) amplitudes of Δi_{α} and Δi_{β} *vs* number of short-circuited turns.

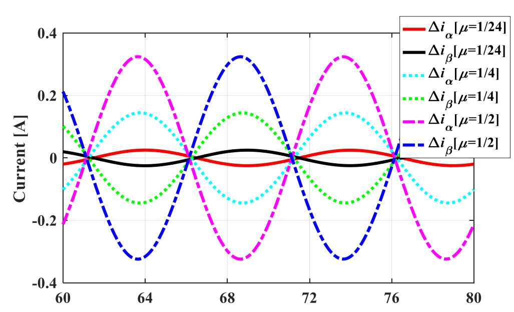

Fig. 10 Δi_{α} and Δi_{β} for different μ. The load currents are i_d = 0A, i_q = 2A, and the rotor speed is 1500rpm.

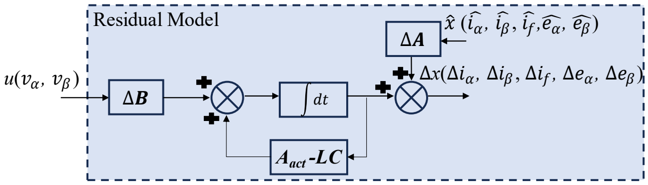

Fig. 11 Block diagram of residual model.

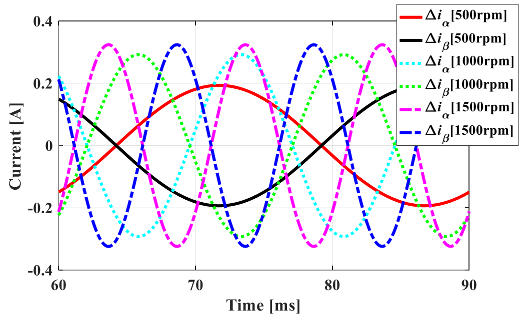

Fig. 12 Δi_α and Δi_β for different speeds. The load currents are i_d = 0A, i_q = 2A, and μ = 0.5.

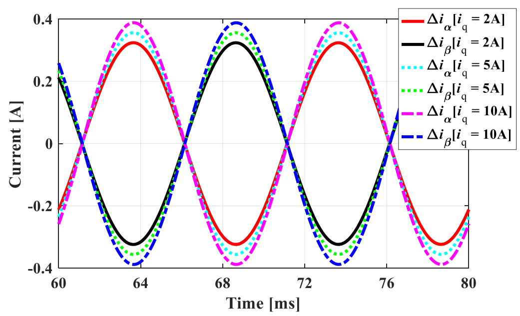

Fig. 13 Δi_α and Δi_β for different load currents. The the rotor speed is 1500rpm, and μ = 0.5.

IV. Faulted Phase Identification

If the ITSC fault is detected using the proposed method, determining the faulted phase becomes crucial as it facilitates the subsequent machine repairs. The process for determining the faulted phase is shown in Fig. 14, as detailed below:

- **Step 1**: μ is assumed to be *1/N*, where *N* represents the total number of turns in one coil.
- **Step 2**: Assign the value of μ to three sets of observer matrices $\boldsymbol{A_{est}}$ and $\boldsymbol{B_{est}}$, which assume the ITSC fault occurs in phases A, B and C, respectively. It should be noted that if the fault is in phase B or C, the same modeling method can be employed to derive the specific expressions of $\boldsymbol{A_{est}}$ and $\boldsymbol{B_{est}}$. These expressions differ from those in (9a). With these three sets of observers, the three sets of observed currents ($\hat{i_\alpha}$ and $\hat{i_\beta}$) can be obtained accordingly.
- **Step 3**: For each Luenberger observer, calculate absolute residuals between the observed and measured i_α and i_β. $K_{a,p}$, $K_{b,p}$ and $K_{c,p}$ represent these absolute residuals, assuming an ITSC in phases A, B and C, respectively.
- **Step 4**: Compute the minimum residual K_{min} from the calculated residuals.
- **Step 5:** If $K_{min} = K_{a,p}$, ITSC is in phase A. If $K_{min} = K_{b,p}$, ITSC is in phase B. Otherwise, ITSC is in phase C.

The fault detection strategy illustrated in Fig. 14 involves the simultaneous operation of three sets of observers, each designed

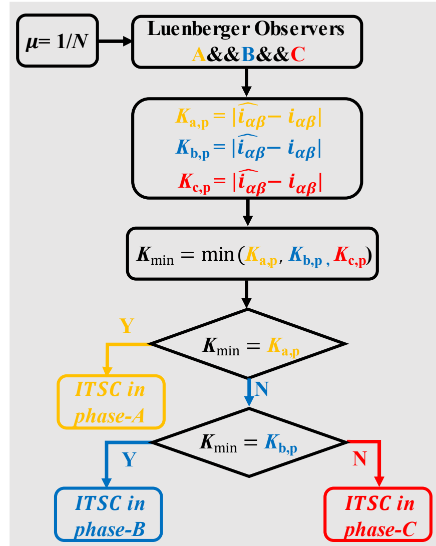

Fig. 14 Flowchart of the faulted phase identification algorithm.

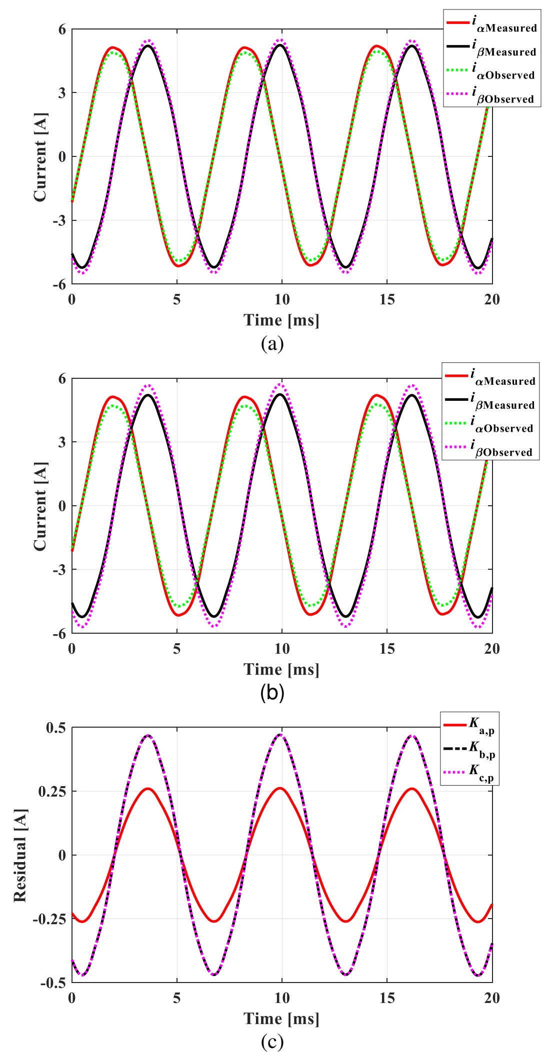

Fig. 15 Measured and observed i_α and i_β. The rotor speed is 1500rpm, the load currents are id = 0A, iq = 5A, μ=1/24 and Rf = 20mΩ. Luenberger observer assuming ITSC in phases (a) A, (b) B, and (c) residuals.

under the assumption that the ITSC fault occurs in a different phase. Consequently, the matrices $\boldsymbol{A_{est}}$ and $\boldsymbol{B_{est}}$ are different

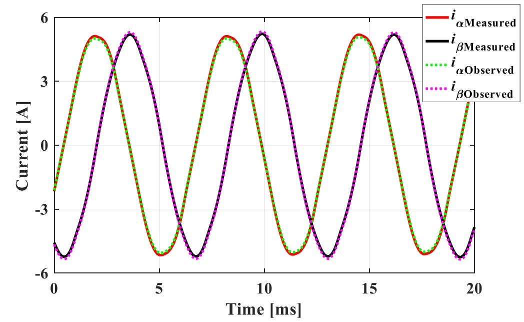

(a)

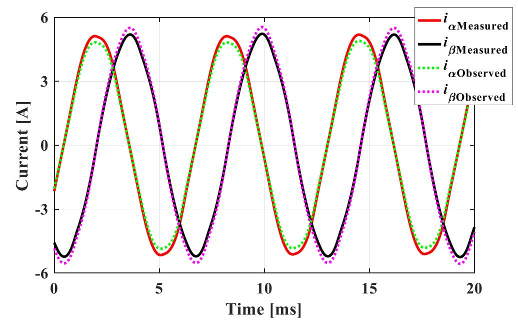

(b)

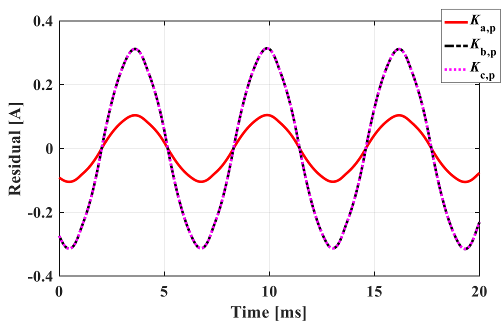

(c)

Fig. 16 Measured and observed i_α and i_β. The rotor speed is 1500rpm, the load currents are i_d = 0A, i_q = 5A, μ = 1/24 and R_f = 0mΩ. Luenberger observer assuming ITSC in phases (a) A, (b) B and (c) residuals

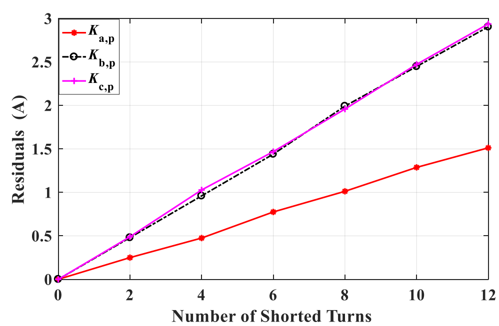

Fig. 17 Residual *vs* number of short-circuited turns. The rotor speed is 1500rpm, the load currents are i_d = 0A, i_q = 5A, and R_f = 0mΩ.

for each observer. The difference between the estimated $\boldsymbol{A_{est}}$ and $\boldsymbol{B_{est}}$ and the actual $\boldsymbol{A_{act}}$ and $\boldsymbol{B_{act}}$ causes discrepancies in the matrices $\Delta\boldsymbol{A}$ and $\Delta\boldsymbol{B}$ [see (13)], making them non-zero. As the deviation of $\Delta\boldsymbol{A}$ and $\Delta\boldsymbol{B}$ from the zero matrix increases, it leads to larger Δi_α and Δi_β. If the fault is indeed located in phase A, the residuals $K_{a,p}$ will exhibit the smallest value, as shown in Fig. 15 and Fig. 16. This is because the residuals between $\boldsymbol{A_{est}}$ and $\boldsymbol{B_{est}}$, obtained under the assumption that the fault is in phase A, and the actual $\boldsymbol{A_{act}}$ and $\boldsymbol{B_{act}}$ are the lowest. In

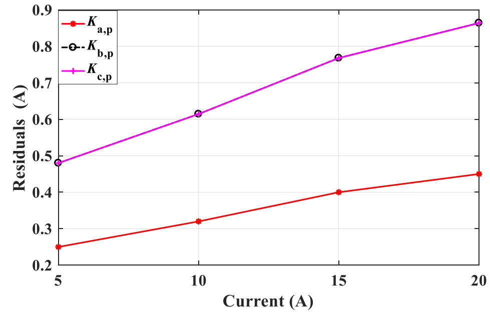

(a)

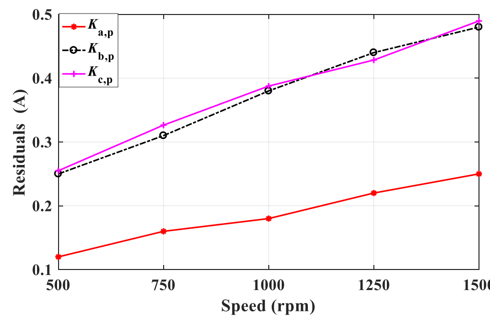

(b)

Fig. 18 Residual *vs* (a) different i_q with rotor speed of 1500rpm and i_d = 0A, and (b) different rotor speeds with i_d = 0A, i_q =5A. In both cases, μ=1/24 and R_f = 20mΩ.

addition, Fig. 17 indicate that the greater the number of turns being short-circuited, the deviation between of $K_{a,p}$, $K_{b,p}$ and $K_{c,p}$ becomes larger, making fault detection more easily.

It is also observed from Fig. 15 (c) and Fig. 16 (c) that $K_{b,p}$ and $K_{c,p}$ are nearly identical. This is attributed to the fault being located in phase A. Consequently, the deviations ΔA and ΔB (assuming faults in phases B and C, respectively) are similar due to the inherent symmetry of the PM machine. In addition, Fig. 15 and Fig. 16 demonstrate that the proposed faulted phase identification strategy is effective not only in identifying the faulted phase at the fully shorted stage (R_f = 0) but also at a very early stage ($R_f \neq 0$). This conclusion can be easily extended to faults occurring in phase B or C. Furthermore, the experiments show that higher load currents and speed result in greater Δi_α and Δi_β values, as shown in Fig. 18, making it easier to detect ITSC faults even at the early stage of ITSC fault with contact resistance (μ=1/24 and R_f= 20mΩ). This conclusion is consistent with the findings in section III.C.

V. Conclusion

The proposed fault detection method in this paper demonstrates that the residuals between the observed currents in the α- and β-axes, obtained from the designed Luenberger observer assuming that the machine is healthy, and their corresponding measured values in the machine are utilized as fault indicators. These indicators can identify ITSC faults both at the early stage, marked by contact resistance, and at the fully shorted stage. Additionally, factors affecting the current residuals have been explored. The findings of this paper indicate that the higher the fault ratio, rotor speed, and load current are, the larger the residuals will be, making detection easier.

In comparison to existing Luenberger observer-based fault diagnostic methods in the literature, which often fail to identify the faulty phase, this paper independently designs three sets of Luenberger observers. Each set assumes the occurrence of ITSC faults in phases A, B, and C, facilitating the identification of the faulted phase.

REFERENCES

[1] J. G. Cintron-Rivera, S. N. Foster, and E. G. Strangas, "Mitigation of turn-to-turn faults in fault tolerant permanent magnet synchronous motors," *IEEE Trans. Energy Convers*., vol. 30, no. 2, pp. 465-475, Jun. 2015.

[2] F. Briz, M. W. Degner, A. Zamarron, and J. M. Guerrero, "Online stator winding fault diagnosis in inverter-fed AC machines using high-frequency signal injection," *IEEE Trans. Ind. Appl*., vol. 39, no. 4, pp. 1109-1117, Jul.-Aug. 2003.

[3] J. Yang, J. Cho, S. B. Lee, J. Y. Yoo and H. D. Kim, "An advanced stator winding insulation quality assessment technique for Inverter-Fed Machines," *IEEE Trans. Ind. Appl.*, vol. 44, no. 2, pp. 555-564, Mar.-Apr. 2008.

[4] J. Hang, W. Sun, Q. Hu, X. Ren, and S. Ding, "Integration of Interturn Fault Diagnosis and Fault-Tolerant Control for PMSM Drive System," *IEEE Trans. Transp. Electrific.,* vol. 8, no. 2, pp. 2825-2835, Jun. 2021.

[5] J. Faiz and H. Nejadi-Koti, "Demagnetization fault indexes in permanent magnet synchronous motors—An overview," *IEEE Trans. Magn.*, vol. 52, no. 4, pp. 1-11, Apr. 2016.

[6] B. Gu, J. H. Choi, and I. Jung, "Development and analysis of interturn short fault model of PMSMs with series and parallel winding connections," *IEEE Trans. Power. Electron.*, vol. 29, no. 4, pp. 2016-2026, Apr. 2014.

[7] Y. Xu, Z. Zhang, Y. Jiang, J. Huang, and W. Jiang, "Numerical analysis of turn-to-turn short circuit current mitigation for concentrated winding permanent magnet machines with series and parallel connected windings," *IEEE Trans. Ind. Electron.,* vol. 67, no. 11, pp. 9101-9111, Nov. 2020.

[8] Y. Fu, Z. Ren, S. Wei, Y. Xu, and F. Li, "Using flux linkage difference vector in early inter-turn short circuit detection for the windings of offshore wind DFIGs," *IEEE Trans. Energy Convers.*, vol. 36, no. 4, pp. 3007-3015, Dec. 2021.

[9] H. Zhou, W. Zhao, H. G. Liu, R. Cheng, and Y. Xie, "Remedial field-oriented control of five-phase fault-tolerant permanent-magnet motor by using reduced-order transformation matrices," *IEEE Trans. Ind. Electron.*, vol. 64, no. 1, pp. 169-178, Jan. 2017.

[10] D. Wei, K. Liu, W. Hu, X. Peng, Y. Chen and R. Ding, "Short-time adaline based fault feature extraction for inter-turn short circuit Diagnosis of PMSM via residual insulation monitoring," *IEEE Trans. Ind. Electron.,* vol. 70, no. 3, pp. 3103-3114, Mar. 2023.

[11] H. Jeong, S. Moon, and S. W. Kim, "An early stage interturn fault diagnosis of PMSMs by using negative-sequence components," *IEEE Trans. Ind. Electron.,* vol. 64, no. 7, pp. 5701-5708, Jul. 2017.

[12] Z. Ullah and J. Hur, "Analysis of inter-turn-short fault in an FSCW IPM type brushless motor considering effect of control drive," *IEEE Trans. Ind. Appl.,* vol. 56, no. 2, pp. 1356-1367, Mar.-Apr. 2020.

[13] J. C. Urresty, J. R. Riba, and L. Romeral, "Diagnosis of interturn faults in PMSMs operating under nonstationary conditions by applying order tracking filtering," *IEEE Trans. Power. Electron.*, vol. 28, no. 1, pp. 507-515, Jan. 2012.

[14] J. Hang, J. Zhang, M. Cheng, B. Zhang, and S. Ding, "High-resistance connection detection in permanent magnet synchronous machine using zero-sequence current component," *IEEE Trans. Power. Electron.*, vol. 31, no. 7, pp. 4710-4719, Jul. 2016.

[15] M. Alam and S. Payami, "A novel control-independent online fault diagnosis of interturn short circuits in SRMs using signal injection technique," *IEEE Trans. Ind. Electron.*, vol. 70, no. 3, pp. 2157-2167, Mar. 2023.

[16] Z. Xu, J. Zhang, and M. Cheng, "Investigation of signal injection methods for fault detection of PMSM drives," *IEEE Trans. Energy Convers*.,vol. 37, no. 3, pp. 2207–2216, Sep. 2022.

[17] J. Zhang, Z. Xu, J. Wang, J. Zhao, Z. Din, and M. Cheng, "Detection and discrimination of incipient stator faults for inverter-fed permanent magnet synchronous machines," *IEEE Trans. Ind. Electron*.,vol. 68, no. 8, pp. 7505–7515, Aug. 2021.

[18] J. C. Urresty, J. R. Riba, and L. Romeral, ''Influence of the stator windings configuration in the currents and zero-sequence voltage harmonics in permanent magnet synchronous motors with demagnetization faults,'' *IEEE Trans. Magn.*, vol. 49, no. 8, pp. 4885–4893, Aug. 2013.

[19] J. C. Urresty, J. R. R. Ruiz, M. Delgado, and L. Romeral, ''Detection of demagnetization faults in surface-mounted permanent magnet synchronous motors by means of the zero-sequence voltage component,'' *IEEE Trans. Energy Convers.*, vol. 27, no. 1, pp. 42–51, Mar. 2012.

[20] H. Lee, H. Jeong, G. Koo, J. Ban, and S. W. Kim, " Attention RNN based severity estimation method for interturn short-circuit fault in PMSMs," *IEEE Trans. Ind. Electron*., vol. 68, no. 4, pp. 3445–3453, Apr. 2021.

[21] Z. Xu, C. Hu, F.Yang, S. Kuo, C. Goh, A. Gupta and A. Nadarajan "Data-Driven inter-turn short circuit fault detection in induction machines," *IEEE Access*, vol. 5, pp. 25055-25068, Oct. 2017.

[22] T. Orlowska-Kowalska, M. Wolkiewicz, P. Piezrzak, M. Skowron, P. Ewert, G. Tarchala, M. Krzysztofiak, and C. Kowalski, , "Fault diagnosis and Fault-Tolerant Control of PMSM Drives–State of the Art and Future Challenges," *IEEE Access*, vol. 10, pp. 59979-60024, 2022.

[23] A. Accetta, M. Cirrincione, M. Pucci, and G. Vitale, "Neural sensorless control of linear induction motors by a full-order Luenberger observer considering the end effects," *IEEE Trans. Ind. Appl*., vol. 50, no. 3, pp. 1891-1904, May. -Jun, 2013.

[24] A. Mahmoudi, I. Jlassi, A. J. M. Cardoso, K. Yahia, and M. Sahraoui, "Inter-turn short-circuit faults diagnosis in synchronous reluctance machines, using the Luenberger state observer and current's second-order harmonic," *IEEE Trans. Ind. Electron.,* vol. 69, no. 8, pp. 8420-8429, Aug. 2022.

[25] S. Bouslimani, S. Drid, L. Chrifi-Alaoui, and L. Delahoche, "On line inter-turn short-circuit fault diagnosis and nonlinear control of PMSM," *In Proc 19th International Multi-Conference on Systems, Signals and Devices*, pp. 1139-1143 May. 2022.

[26] V. Dinkhauser and F. W. Fuchs, "Rotor turn-to-turn faults of doubly-fed induction generators in wind energy plants-modelling, simulation and detection," in *Proc. 13th Eur. Conf. Power Electron. Appl.,* pp. 1819-1826: Sep. 2008.

[27] S. Nadarajan, S. K. Panda, B. Bhangu, and A. K. Gupta, "Online model-based condition monitoring for brushless wound-field synchronous generator to detect and diagnose stator windings turn-to-turn shorts using extended Kalman filter," *IEEE Trans. Ind. Electron.,* vol. 63, no. 5, pp. 3228-3241, May. 2016.

[28] Y. Qin, G. J. Li, C. Jia, and P. J. Mckeever, "PWM Voltage-based modeling for PM machines with inter-turn short circuit fault considering the effect of drives," *IEEE Trans. Ind. Electron*., vol. 70, no. 11, pp. 10981-10991, Nov. 2023.

[29] A. Andersson and T. Thiringer, "Motion sensorless IPMSM control using linear moving horizon estimation with Luenberger observer state feedback," *IEEE Trans. Transp. Electrific.,* vol. 4, no. 2, pp. 464-473, Jun. 2018.